

## Estimation of CO<sub>2</sub> Content in the Gas Phase of Melt Inclusions Using Raman Spectroscopy: Case Study of Inclusions in Olivine from the Karymsky Volcano (Kamchatka)

N.L. Mironov<sup>a</sup> ✉, D.P. Tobelko<sup>a</sup>, S.Z. Smirnov<sup>b,c</sup>, M.V. Portnyagin<sup>a,d</sup>, S.P. Krasheninnikov<sup>a</sup>

<sup>a</sup> Vernadsky Institute of Geochemistry and Analytical Chemistry, Russian Academy of Sciences, ul. Kosygina 19, Moscow, 119991, Russia

<sup>b</sup> V.S. Sobolev Institute of Geology and Mineralogy, Siberian Branch of the Russian Academy of Sciences, pr. Akademika Koptyuga 3, Novosibirsk, 630090, Russia

<sup>c</sup> Novosibirsk State University, ul. Pirogova 1, Novosibirsk, 630090, Russia

<sup>d</sup> GEOMAR Helmholtz Centre for Ocean Research Kiel, Wischhofstr. 1-3, 24148 Kiel, Germany

Received 5 May 2019; accepted 28 August 2019

**Abstract**—Carbon dioxide (CO<sub>2</sub>) is one of the main volatile components of natural magmas, but estimation of its initial contents remains a challenge. Study of melt inclusions in minerals permits a direct estimation of the content of CO<sub>2</sub> in the melts. For the precise determination of its content in melt inclusions, it is necessary to analyze the contents of CO<sub>2</sub> both in glass and in the fluid daughter phase of the inclusions. In this work, we constructed a calibration dependence of the density of CO<sub>2</sub> in the range 0.01–0.22 g/cm<sup>3</sup> on the distance between its characteristic peaks in Raman spectra (Fermi diads). The accuracy of density determination is ±0.03 g/cm<sup>3</sup>. The calibration plot was used to estimate the density of CO<sub>2</sub> in the gas phase of melt inclusions in magnesian olivine (Fo<sub>84.8–88.5</sub>) from basalts of the Karymskii Volcano, eastern Kamchatka. The estimated density was 0.03–0.21 g/cm<sup>3</sup>. Using these values, we have first evaluated the minimum initial content of CO<sub>2</sub> in the parental magmas of the Karymskii Volcano, 0.45 wt.%. These data, along with the known initial content of water (~4.5 wt.%), indicate that the parental magmas began to crystallize at a pressure of at least 7 kbar (depth of >25 km). To increase the reliability of the above method of estimation of the CO<sub>2</sub> content in the gas phase of olivine-hosted melt inclusions, we propose to carry out preliminary experimental reheating of inclusions for the complete homogenization of the fluid phase and determination of the 3D size of melt inclusions. The performed study provides a reliable evaluation of the content of CO<sub>2</sub> in parental magmas, the depth of crystallization, and the degree of magma degassing and permits a comparison of the compositions of magmatic fluids and high-temperature volcanic gases.

**Keywords:** olivine-hosted melt inclusions, gas bubble, Raman spectroscopy, CO<sub>2</sub>, parental magmas, subduction zones

### INTRODUCTION

Carbon dioxide (CO<sub>2</sub>) is one of the main fluid components of both moderately reduced and oxidized natural magmas, including island-arc magmas (Wallace, 2005). Since the solubility of CO<sub>2</sub> depends strongly on pressure (Blank and Brooker, 1994), CO<sub>2</sub> degassing of magma begins at a significant depth. Melt inclusions in olivine from primitive island-arc rocks are the only source of direct information about the content of volatiles in parental magmas (Sobolev, 1996; Wallace, 2005; Portnyagin et al., 2007). This is because the melt inclusion is isolated by the host mineral from the surrounding magma and can preserve the volatile components. In contrast to melt inclusions, the erupted magmas (rocks) are significantly degassed during their ascent to the surface

and eruption. Melt inclusions in olivine are potentially capable to preserve the initial amounts of CO<sub>2</sub>, because the rate of CO<sub>2</sub> diffusion in olivine is very slow (<10<sup>-12</sup> cm<sup>2</sup>/s at 1250–1400 °C) (Tingle et al., 1988). In the course of the melt inclusions evolution, the internal pressure decreases and a daughter fluid phase forms (Danyushevsky et al., 2002; Schiano, 2003; Wallace et al., 2015). A significant portion of CO<sub>2</sub> initially dissolved in the melt is redistributed into the fluid phase. At the same time, the residual melt is depleted in this volatile component (Mironov and Portnyagin, 2011; Steele-MacInnis et al., 2011; Bucholz et al., 2013; Aster et al., 2016). The bulk CO<sub>2</sub> content in melt inclusions, determined most often by analysis of CO<sub>2</sub> in residual glass, is usually underestimated (Mironov et al., 2015). The degree of this underestimation varies for different objects and samples and can exceed 90% (Mironov et al., 2015; Moore et al., 2015; Wallace et al., 2015; Aster et al., 2016). The investigations of the fluid regime of island-arc magmas, taking

✉ Corresponding author.

E-mail address: nmironov@geokhi.ru (N.L. Mironov)

into account the CO<sub>2</sub> content in the glass and fluid phase of melt inclusions, are few and usually do not aim at estimating the CO<sub>2</sub> content in the most primitive magmas (Mironov et al., 2015; Moore et al., 2015, 2018; Aster et al., 2016; Robidoux et al., 2018). Such data are missing for Kamchatka volcanoes (Naumov et al., 2020), except for Klyuchevskoi (Mironov et al., 2015; Moore et al., 2018).

Three methods are used to take account of the CO<sub>2</sub> content in a gas bubble and to estimate the total CO<sub>2</sub> content in melt inclusions: (1) calculation of the composition and amount of equilibrium fluid (Steele-MacInnis et al., 2011; Wallace et al., 2015; Aster et al., 2016; Moore et al., 2018; Tucker et al., 2019), (2) experimental homogenization of inclusions (Mironov et al., 2015; Wallace et al., 2015), and (3) mass balance calculation based on the estimated proportions

of glass and gas phase and their CO<sub>2</sub> contents (Naumov et al., 2006; Steele-MacInnis et al., 2011; Hartley et al., 2014; Moore et al., 2015; Aster et al., 2016; Robidoux et al., 2018; Taracsak et al., 2019). Raman spectroscopy is used to determine the CO<sub>2</sub> content in the gas phase, which is usually a low-density fluid (Steele-MacInnis et al., 2011; Hartley et al., 2014; Moore et al., 2015).

Each of the proposed methods has its advantages and disadvantages, which are analyzed by Moore et al. (2018). In particular, the advantage of the mass balance method (the further development of which this research is aimed at) is its relative simplicity. Along with Raman spectroscopy and ion probe microanalysis, this method permits one to study a large number of inclusions and to obtain statistically significant results. A disadvantage of this method is the frequent occurrence of carbonate on the walls of gas bubbles in naturally quenched inclusions (Kamenetsky et al., 2002; Moore et al., 2015; Aster et al., 2016; Robidoux et al., 2018), which cannot be taken into account in measurements and calculations. Imprecise estimation of the bubble and melt inclusion volumes also contributes to a large error in the calculation. The melt inclusion volume is usually estimated on the basis of optical measurements in one plane and on the assumption that the inclusion is an ellipsoid with two equal axes (the vertical axis  $z$  is equal to the visible width  $y$ ) (Moore et al., 2018).

The goal of this work was to develop and improve the techniques of Raman spectroscopy estimation of the density of CO<sub>2</sub> in the gas phase of melt inclusions at the Institute of Geology and Mineralogy, Novosibirsk, and to compare the volumes of melt inclusions and their bubbles estimated from results of optical measurements in one plane (2D) and two planes (3D) in order to improve the accuracy of estimation of the bulk content of CO<sub>2</sub> in melt inclusions. The technique was tested on a series of inclusions in olivine (Fo<sub>84.8-88.5</sub>) from basalt of the Karymsky Volcano in eastern Kamchatka (Grib and Perepelov, 2008; Tobelko et al., 2019). The data obtained are used to estimate the minimum initial content of CO<sub>2</sub> in parental melts as well as the pressure and depth of their crystallization.

## METHODS

**Raman spectroscopy.** The key task of mass balance calculation of the total CO<sub>2</sub> content in melt inclusions is to determine the CO<sub>2</sub> content in their gas phase. In this work, the density of CO<sub>2</sub> in the gas phase was determined by Raman spectroscopy. The method is based on the accurate measurement of the position of two characteristic vibration peaks of CO<sub>2</sub> molecules (so-called “Fermi diads”) at ~1285 and ~1388 cm<sup>-1</sup> and the direct dependence of the distance between the peaks (the difference in wavenumbers) on the CO<sub>2</sub> density (Frezzotti, 2012) (Fig. 2).

The measurements were performed at the Institute of Geology and Mineralogy, Novosibirsk, using a Horiba

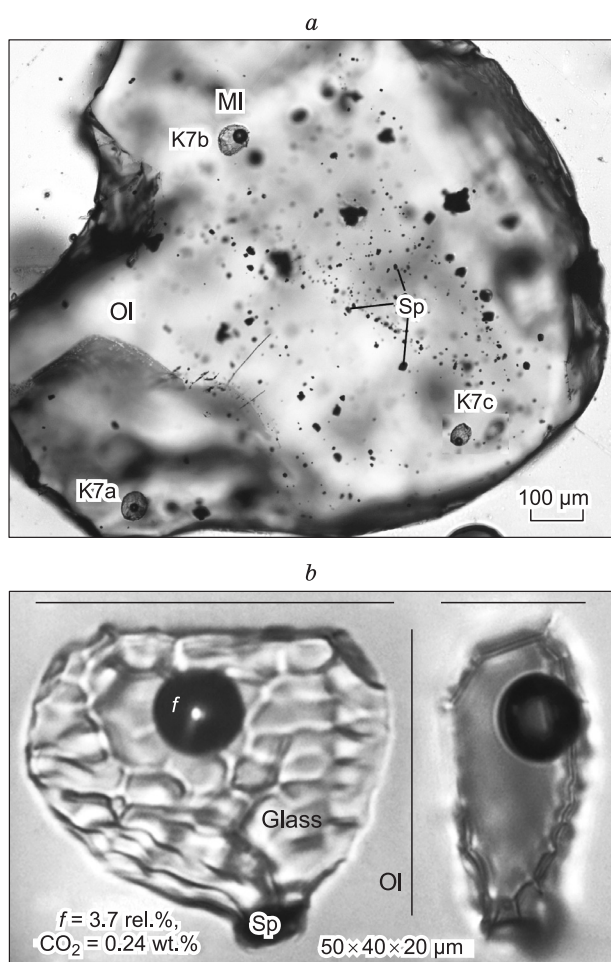


**Fig. 1.** Micrographs of experimentally reheated and quenched olivine-hosted melt inclusions from the Karymsky Volcano. *a*, Typical olivine grain (K7) containing melt inclusions (MI) (K7a, K7b, and K7c; Table 1) and numerous small crystalline chrome spinel inclusions (SP). The same melt inclusions are shown in Fig. 2 together with Raman spectra of their fluid bubbles; *b*, melt inclusion K4 (Table 1), consisting of glass (GL) and bubble ( $f$ ), in two orthogonal cross sections. In contrast to most of the studied melt inclusions, K4 is a flattened inclusion with a thickness twice as small as the width, which one must take into account for precise estimation of the gas bubble contribution to the total CO<sub>2</sub> content in the melt inclusion (Fig. 5).

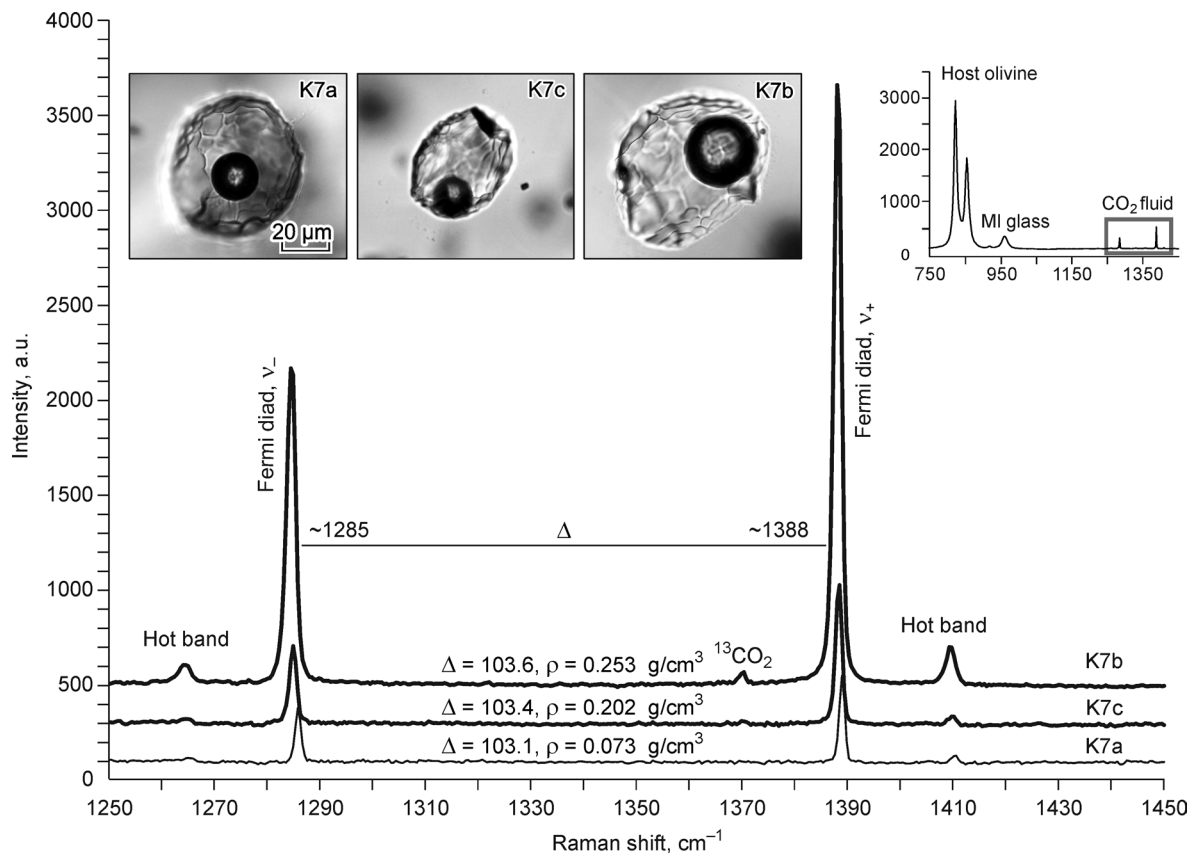


**Fig. 2.** Raman spectra of gas bubbles in melt inclusions from the Karymsky Volcano, with characteristic peaks of CO<sub>2</sub> (Fermi diads at ~1285 and ~1388 cm<sup>-1</sup>). Spectra for three melt inclusions are shown: K7a is a low-density gas bubble in melt inclusion with calculated CO<sub>2</sub> = 0.11 wt.%; K7c is a denser gas bubble in melt inclusion, with calculated CO<sub>2</sub> = 0.45 wt.%, which is the maximum content of CO<sub>2</sub> in the studied melt inclusions from the Karymsky Volcano; K7b is the densest and largest gas bubble in melt inclusion, with calculated CO<sub>2</sub> = 1.9 wt.%, which indicates a heterogeneous (melt + fluid) trapping of the melt inclusion and does not represent the true melt composition (see also Fig. 5 and Table 1). Inset shows Raman spectra (750–1450 cm<sup>-1</sup>) of the host olivine and glass and a gas bubble in the melt inclusion bul12 used for calibration ( $\rho = 0.14$  g/cm<sup>3</sup>).

Labram HR800 Raman spectrometer with a solid-state laser (excitation at 532 nm, 50 mW) and a semiconductor detector (CCD matrix) cooled by the Peltier method. The measurements were carried out for melt inclusions located at different depths from the olivine surface in the centers of their gas bubbles.

High spatial resolution was provided by an Olympus BX-41 confocal microscope. High spectral resolution was achieved by using a holographic diffraction grating with 1800 grooves/mm. The diameter of the studied gas bubbles in melt inclusions varied from 10 to 35 microns (Table 1). The measurements were made with a confocal aperture 200  $\mu$ m in diameter, which ensured a high sensitivity and shortened the signal integration time. The high-sensitivity detector allows analysis of smaller gas bubbles or fluid inclusions using a confocal aperture of smaller diameter. Analysis of such samples requires more time to accumulate the signal, but the spectrum quality remains almost unchanged.

Initial calibration was performed against the characteristic 585.25 nm line in the neon spectrum. The CO<sub>2</sub> spectra were measured in one window in the interval 1250–1450 cm<sup>-1</sup>.

The presence of other gases in the fluid bubbles was checked for half of the studied melt inclusions in the intervals 1100–1200 cm<sup>-1</sup> (SO<sub>2</sub>); 2280–2380 cm<sup>-1</sup> (H<sub>2</sub>S); 2550–2650 cm<sup>-1</sup> (N<sub>2</sub>); and 2900–2930 cm<sup>-1</sup> (CH<sub>4</sub>). None of the analyzed bubbles had detectable amounts of gases other than CO<sub>2</sub> (Table 1). The integration time of one spectrum was 5 s; one analysis included 6 integrations. The spectra were processed by the Origin 8.0 program. Each line of the Fermi diad was processed separately. The straight line going through the average values of the background noise was taken as a baseline. The baseline was subtracted before approximation. Each line of Fermi diad was approximated by a Gaussian or a Lorentzian function. The exact wavenumber of the line was determined at the half width of the approximated peak. The correctness of approximation was verified by the close coincidence of the approximated line and the measured spectrum.

Eight gas bubbles in olivine-hosted melt inclusions with a density between 0.013 and 0.22 g/cm<sup>3</sup> from the Klyuchevskoi Volcano were used as reference samples. The densities of CO<sub>2</sub> in these inclusions were previously estimated

**Table 1.** The size of melt inclusions (MI) and the density and content of CO<sub>2</sub> in gas bubbles of the melt inclusions in olivine from the Karymsky Volcano

MI	T <sub>q</sub> , °C	MI			Bubble			Relative volume of bubble, %			Distance between Fermi diads, ΔF, cm <sup>-1</sup>	Density of CO <sub>2</sub> , g/cm <sup>3</sup>	Content of CO <sub>2</sub> , wt. %	Fo olivine, mol. %	Other gases	
		x	y	z1	z2	d, μm	(x, y, z1)	(x, y, z2)	x, y, z = y	x, y, z = x/2 + y/2						x, y, z = x/2 + y/2
K-06-6	1300	50	30	–	46	15	–	4.9	7.5	5.6	5.3	103.06	0.066	0.126	–	N.d.
K-06-8	–	100	70	–	56	28	–	5.6	4.5	3.7	3.6	103.04	0.058	0.127	88.5	N.d.
K1a	1170	50	36	34	30	13	3.6	4.1	3.4	2.8	2.8	102.98	0.033	0.051	–	N.d.
K1b	1170	76	66	57	54	20	2.8	3.0	2.4	2.2	2.2	102.99	0.040	0.045	85.9	N.d.
K2	1170	75	54	54	58	22	4.9	4.5	4.9	4.1	4.0	103.15	0.099	0.173	86.9	N.d.
K4	1170	50	40	20	20	11.5	3.8	3.8	1.9	1.7	1.7	103.33	0.167	0.244	85.9	N.a.
K6	1170	54	45	50	58	17	4.0	3.5	4.5	4.1	4.1	103.11	0.083	0.112	84.8	N.a.
K7a	1170	60	52	45	54	19	4.5	3.8	3.9	3.6	3.6	103.08	0.073	0.105	–	N.d.
K7b	1170	70	55	35	32	29.5×24	18.9*	17.0	12.1*	10.7*	10.5*	103.56	0.253	1.874	–	N.a.
K7c	1170	46	37	44	46	16.5	6.0	5.7	7.1	6.4	6.3	103.42	0.202	0.454	88.4	N.a.
K9b	1170	37	30	29	34	10.5	3.7	3.1	3.5	3.1	3.1	103.37	0.183	0.214	–	N.a.
K9e	1170	40	35	29	35	12	4.3	3.5	3.5	3.3	3.3	103.41	0.196	0.265	–	N.a.
K9d	1170	50	42	39	46	15.5	4.6	3.9	4.2	3.9	3.8	103.34	0.171	0.254	88.0	N.a.
K12	1170	53	40	47	40	14.5	3.1	3.6	3.6	3.1	3.0	103.09	0.074	0.102	86.7	N.d.
K13	1170	125	90	71	70	35	5.4	5.4	4.2	3.5	3.5	103.45	0.211	0.449	88.5	N.a.
K14	1170	45	40	47	50	15	4.0	3.8	4.7	4.4	4.4	103.13	0.090	0.130	–	N.d.

Note. Length (x), width (y), and thickness (z) of melt inclusions are given according to the data of optical measurements in one section (z1) and measurements in two orthogonal sections (z2). The bold-typed values are the most precise estimates. The asterisked values for the inclusion K7b were obtained under assumption of the spherical shape of a fluid bubble with a diameter of 29.5 μm. The composition of the host olivine for representative inclusions (Fo, mol. %) was analyzed with a JEOL JXA 8200 (GEOMAR, Kiel, Germany) electron microprobe under the same conditions as described by Tobelko et al. (2019). Other gases in the bubbles were either not detected (N.d.) or not analyzed (N.a.).

by Raman spectroscopy at Virginia Tech, USA (Moore et al., 2018). These samples were used to determine a correlation between the CO<sub>2</sub> density and the distance between the Fermi diad lines (Fig. 3). The measurements were carried out during two analytical sessions with a four-month gap between them. The calibration plot was stable during the course of this study. It is unique for the applied instrument and the analytical conditions and differs from calibrations used in other laboratories (Fall et al., 2011; Wang et al., 2011; Lamadrid et al., 2017). The derived calibration equation is as follows:

$$\rho\text{CO}_2 \text{ (g/cm}^3\text{)} = 0.3776 \times \Delta F \text{ (cm}^{-1}\text{)} - 38.851, \quad (1)$$

where ΔF is the difference between the wavenumbers of the Fermi diad lines and ρCO<sub>2</sub> is the CO<sub>2</sub> density in the gas phase (Fig. 3).

The reference samples were analyzed in total 2 to 15 times for an individual bubble, and the reproducibility of ΔF (2σ) varied from 0.007 to 0.049 cm<sup>-1</sup> (on average, 0.03 cm<sup>-1</sup>), which corresponds (Eq. 1) to density variations from 0.005 to 0.019 g/cm<sup>3</sup> (on average, 0.011 g/cm<sup>3</sup>). Thus, we estimate the overall uncertainty of the density estimates at ±0.03 g/cm<sup>3</sup>, which includes an external error of 0.020 g/cm<sup>3</sup> (Moore et al., 2018) and the average reproducibility of the reference samples in this study (0.011 g/cm<sup>3</sup>) (Fig. 3).

The gas bubble in each of the melt inclusions from the Karymsky Volcano was analyzed twice, and the results were averaged. The ΔF variations for the two analyses were in the range 0.01–0.03 cm<sup>-1</sup>, which corresponds to the uncertainty of determined density of ≤0.01 g/cm<sup>3</sup>. All selected melt inclusions with gas bubbles for which a clear optical focus was observed were successfully analyzed, regardless of their location in the olivine grain.

This Raman spectroscopy technique was earlier used to determine the CO<sub>2</sub> density in gas bubbles in melt inclusions by non-Russian researchers only (Hartley et al., 2014; Moore et al. 2015, 2018; Robidoux et al., 2018). Our study is the first case of its application at a Russian geological research institute.

**Study of melt inclusions.** The study of melt inclusions included several steps: (1) selection of representative olivine grains with melt inclusions from the >0.5 mm fraction of basaltic scoria from the Karymsky Volcano (Tobelko et al., 2019; sample K6-06); (2) high-temperature experiment on melting of daughter crystal phases in melt inclusions, which contained melt and fluid phase after experiment; (3) mounting olivine grains into epoxy resin and their polishing; preliminary optical measurements of inclusion and gas bubble sizes; (4) Raman measurements, spectrum processing, and calculation of the CO<sub>2</sub> density in bubbles; (5) measurement of the melt inclusion and bubble sizes in the orthogonal sections of olivine grains; (6) mass balance calculation for estimat-

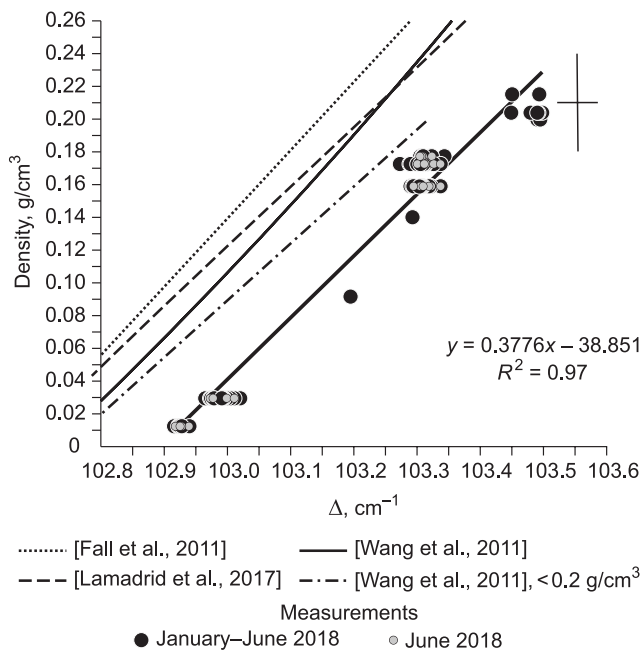


**Fig. 3.** Calibration plot for estimation of the CO<sub>2</sub> density in gas bubbles of melt inclusions as a function of the distance between characteristic CO<sub>2</sub> peaks (Fermi diads). The calibration plot was obtained using a Horiba Labram HR800 Raman spectrometer (532 nm, 1800 grooves/mm) at the Sobolev Institute of Geology and Mineralogy, Novosibirsk, based on the earlier measured density of CO<sub>2</sub> in gas bubbles in melt inclusions from the Kliuchevskoi Volcano (Moore et al., 2018). The error bars (top right) correspond to the average reproducibility of  $\Delta F$  ( $2\sigma$ ,  $0.03 \text{ cm}^{-1}$ ) for reference samples and the overall uncertainty of density determination ( $0.03 \text{ g/cm}^3$ ), see text (Methods, Raman spectroscopy). The obtained calibration is unique for this instrument and the described analytical conditions. The calibration line is shifted relative to the calibration lines obtained in other laboratories under the same or similar conditions (Horiba Labram HR800; 514 nm and 1800 grooves/mm (Fall et al., 2011); 532 nm and 1800 grooves/mm (Wang et al., 2011), with a calibration plot for the entire density range and a linear dependence for the low density region,  $<0.2 \text{ g/cm}^3$ , given by Lamadrid et al. (2017); and 532 nm and 1800 grooves/mm (Lamadrid et al., 2017)). The observed difference confirms the previous conclusion (Lamadrid et al., 2017) that each Raman spectrometer requires an independent calibration.

ing the minimum bulk content of CO<sub>2</sub> in melt inclusions, i.e., the amount of CO<sub>2</sub> in their gas phase, not taking into account the amount of CO<sub>2</sub> in glass.

**Homogenization experiments.** Most of the studied melt inclusions were partially crystallized at room temperature before the high-temperature experiments, and only one of them was a naturally quenched glassy melt inclusion. A high-temperature experiment on remelting of the daughter phases in the partially crystallized melt inclusions was carried out in a vertical Nabertherm RHTV 120-300/17 tube furnace at 1 atm at the Institute of Geochemistry and Analytical Chemistry, Moscow. This furnace allows high-temperature heating in the redox-controlled atmosphere (Krashennnikov et al., 2017). The experimental conditions ( $T=1170 \text{ }^\circ\text{C}$ ,  $f_{\text{O}_2} = \text{QFM} + 1.5$ ,  $t = 5 \text{ min}$ ) were identical to the estimated crystallization parameters ( $T, f_{\text{O}_2}$ ) of the paren-

tal melts of the Karymsky Volcano (Tobelko et al., 2019). An unwelded platinum ampoule with grains was kept in the inert-gas atmosphere at  $\sim 900 \text{ }^\circ\text{C}$  for 5 min before a heating experiment in order to remove air and reach the desired redox conditions. Afterwards, the ampoule was kept at  $1170 \text{ }^\circ\text{C}$  for 5 min and then was dropped in water for quenching (Krashennnikov et al., 2018). After quenching, the inclusions consisted of glass, a gas bubble, and, often, small single crystals of spinel, which were probably trapped by olivine together with melt (Fig. 1). Optical examination showed that the gas bubbles of the heated and experimentally quenched inclusions, in contrast to bubbles in naturally quenched inclusions, were almost free of crystalline phases, except for a few small crystallites of native sulfur and unknown phases.

#### Estimation of the size and volume of melt inclusions.

The literature data on the size of melt inclusions are usually based on the assumption of their three-axis ellipsoid shape (Moore et al., 2015; Aster et al., 2016; Tucker et al., 2019). To estimate the ellipsoid volume, the visible length ( $x$ ) and width ( $y$ ) of inclusions were measured. The thickness ( $z$ ) was assumed to be equal to the inclusion width ( $z = y$ ) (Moore et al., 2015) or to the average of the visible length and width ( $z = x/2 + y/2$ ) (Tucker et al., 2019). In some studies, the volume was calculated under assumption of the spherical shape of melt inclusions (diameter =  $x/2 + y/2$ ) (Mironov et al., 2015). To assess the correctness of such assumptions and the error that they add to the calculation of the inclusion volume, we carried out an additional study (see below).

The thickness of inclusions was estimated by two methods. In the first method, the thickness was measured with a built-in microscope micrometer by focusing on the top and bottom of the inclusion. The fine-ribbed surface of the inclusion walls (Fig. 1b), typical of the studied melt inclusions, made it possible to do this. The obtained values were multiplied by the coefficient corresponding to the average value of the refractive index of olivine  $\text{Fo}_{90-80}$  ( $n_p - n_g$ , 1.65–1.71, on average, 1.68) (Troeger, 1979). The unknown optical orientation and composition of olivine grain introduce an error of 1.8% into the estimated melt inclusion thickness. If the location of either the top or the bottom of an inclusion is optically uncertain, for example, when the inclusion is partly exposed on the surface, the distance from its top or bottom to the plane of the largest cross-section area can be measured.

The second method implied measuring the melt inclusion dimensions in the orthogonal cross sections of olivine grains. For this purpose, after the Raman analysis, the grains with melt inclusions were remounted into epoxy resin so that their polished planes were oriented at a right angle to the mount surface. The grains were then ground and polished again (Fig. 1b). Then, the inclusion dimensions were again measured under microscope. The orthogonal section allowed a direct measurement of the third dimension (thickness,  $z$ ) of the melt inclusion. The error in measurement of

**Table 2.** Mass balance calculation scheme of the CO<sub>2</sub> content in melt inclusion bubble

Calculation steps	1	2	3	4	5
Calculation parameter	$V_{MI}, \mu\text{m}^3$	$V_b, \mu\text{m}^3$ ; $m(\text{CO}_2)_b, \text{pg} (10^{-12} \text{ g})$	$V_g, \mu\text{m}^3$ ; $m_g, \text{pg}$	$m_{MI}, \text{pg}$	$m(\text{CO}_2)_b, \text{wt.}\%$
Calculation formula	$V_{MI} = 4/3 \cdot \pi \cdot x/2 \cdot y/2 \cdot z/2$	$V_b = 4/3 \cdot \pi \cdot (d/2)^3$ ; $m(\text{CO}_2)_b = V_b \cdot \rho$ $\rho$ is CO <sub>2</sub> density, Raman data, $\text{g}/\text{cm}^3 = \text{pg}/\mu\text{m}^3$	$V_g = V_{MI} - V_b$ ; $m_g = V_g \cdot \rho$ ; $\rho = 2.7 \text{ g}/\text{cm}^3$	$m_{MI} = m_g + m(\text{CO}_2)_b$	$m(\text{CO}_2)_b \cdot 100/m_{MI}$

Notes. MI, melt inclusion; *b*, bubble; *g*, glass; *x*, *y*, *z*, linear dimensions of melt inclusion: length, width, and thickness,  $\mu\text{m}$ ; *d*, diameter of bubble,  $\mu\text{m}$ .

the thickness might be due to the nonorthogonal orientation of grains on remounting (in our case, up to  $\sim 10^\circ$ ) and is estimated not to exceed  $-1.5$  rel.%. The melt inclusion volumes were then estimated using a formula for the volume of a three-axis (*x*, *y*, *z*) ellipsoid ( $V = 4/3 \cdot \pi \cdot x/2 \cdot y/2 \cdot z/2$ ). The error in linear microscope measurements was assumed to be  $\pm 2 \mu\text{m}$ . In the cases when the shape of the inclusion differed significantly from ellipsoidal, e.g., for the inclusion K13 being a flattened truncated cone, an error of  $\pm 5 \mu\text{m}$  was taken.

Despite their simplicity, 3D optical measurements and study of melt inclusion shapes are unknown in literature, although similar studies were carried out for examining the morphology of heterogeneous fluid inclusions (Bakker and Diamond, 2006).

**Mass balance calculations.** To determine the mass fraction of CO<sub>2</sub> in the gas phase of inclusions, we applied a common mass balance calculation scheme (Hartley et al., 2014; Moore et al., 2015; Moore and Bodnar, 2019). This scheme includes a subsequent calculation of: (1) the volume of melt inclusion, (2) the mass of CO<sub>2</sub> in the bubble, based on the bubble volume and the CO<sub>2</sub> density estimated by Raman spectroscopy, (3) the volume and mass of glass in the melt inclusion (the glass density was assumed to be  $2.7 \text{ g}/\text{cm}^3$  (Shishkina et al., 2010)), (4) the total mass of the melt inclusion (glass + bubble), and (5) the mass fraction of CO<sub>2</sub> in the gas phase (Table 2). If the content of CO<sub>2</sub> in the glass is known, the total content of CO<sub>2</sub> in the melt inclusion can be calculated as a sum of the measured CO<sub>2</sub> content in the glass and the calculated CO<sub>2</sub> content in the gas phase. If the content of CO<sub>2</sub> in the glass is unknown (as in this study), the mass fraction of CO<sub>2</sub> in the bubble is regarded as the minimum total CO<sub>2</sub> content in the melt inclusion (Table 1). The total CO<sub>2</sub> contents of melt inclusions estimated from the ion probe data (SIMS) for glass and from the Raman spectroscopy data for fluid bubbles will be presented in next publications.

## RESULTS

**Types of inclusions, their size and volume.** The studied melt inclusions were single or multiple in olivine grain (Fig. 1a), without a regular location. A characteristic feature of the studied olivines was also the presence of numerous scattered small crystalline spinel inclusions (Fig. 1a). All except for one of the studied olivine-hosted melt inclusions

were experimentally quenched. They consisted of glass and a gas bubble and usually contained small single spinel crystals (Fig. 1b). In most of the experimentally quenched melt inclusions, there were occasional or no crystalline phases on the walls of gas bubbles. However, abundant crystalline phases were present on the walls of a low-density ( $0.06 \text{ g}/\text{cm}^3$ ) gas bubble in a naturally quenched inclusion (K-06-8, Table 1). Although the phases were not studied by Raman spectroscopy, some of them might be carbonates (Kamenetsky et al., 2002; Moore et al., 2018; Robidoux et al., 2018). Noteworthy, the olivine hosting this naturally quenched inclusion has a high-Fo (Fo<sub>88.5</sub>) composition, like the olivines hosting two reheated inclusions with the highest bubble densities ( $0.20$ – $0.21 \text{ g}/\text{cm}^3$ ), but the gas bubble density in this inclusion is much lower ( $0.06 \text{ g}/\text{cm}^3$ ). This difference is in agreement with crystallization of daughter carbonate phases on the walls of a gas bubble in the naturally quenched inclusion.

The size of the melt inclusions varied (average length *x*, width *y*, and thickness *z*) from  $35$  to  $95 \mu\text{m}$ , and the diameter of gas bubbles, from  $10$  to  $35 \mu\text{m}$ . Most of the melt inclusions had a smooth oval or short-prism shape and characteristic finely ribbed walls (Fig. 1). The average length-to-width ratio is  $1.3$ , and the width-to-thickness ratio is  $1$  (Table 1), as assumed in many research works (Moore et al., 2015, 2018; Aster et al., 2016; Taracsak et al., 2019). In some inclusions, however, the width-to-thickness ratio varies from  $0.7$  to  $2.0$ , reaching a maximum in flattened inclusions (Fig. 1b,  $y/z = 2$ ). The gas bubbles in the melt inclusions were near-spherical, with the difference among the diameters in three directions not exceeding  $5$  rel.%. One melt inclusion contained a flattened gas bubble (K7b is a heterogeneously trapped inclusion, melt + fluid, Fig. 2; Table 1).

The volume fractions of gas bubbles in the studied melt inclusions, which are estimated from 3D measurements of the inclusions (*x*, *y*, *z*), vary from  $2.8$  to  $6.0$  vol. % (on average,  $4.2$  vol.%) (Figs. 4 and 5; Table 1). The largest bubbles ( $5.4$ – $5.7$  vol.%) are typical of inclusions in the most magnesian olivines (Fo<sub>88.4–88.5</sub>). The inclusions from more Fe-rich olivines contain smaller bubbles (Table 1). One melt inclusion differs from the other in a significantly larger volume of the gas bubble ( $17$  vol.%) (Fig. 4a). The linear correlation between the volumes of melt inclusions and their gas bubbles (Frezotti, 2001) and the volume fractions of bubbles not

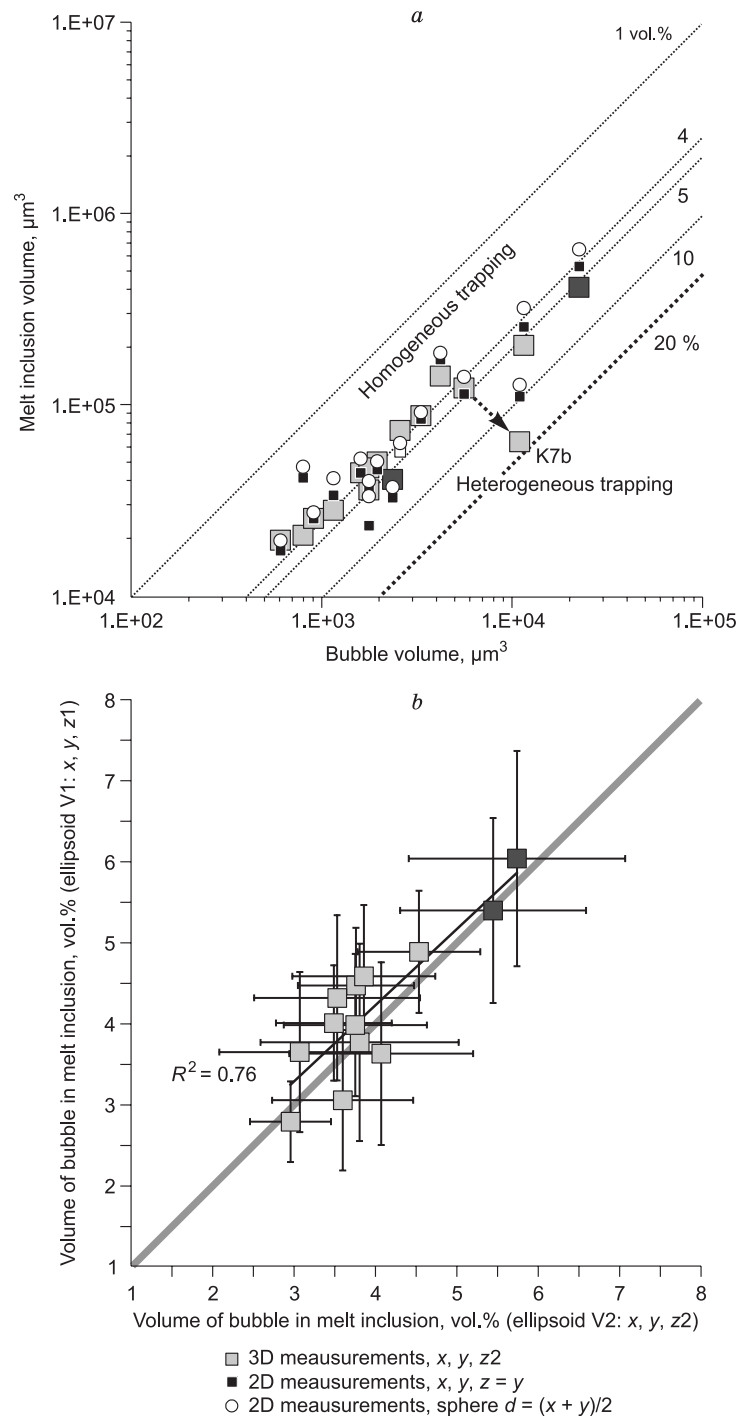


**Fig. 4.** Correlation between the volumes of studied melt inclusions and their gas bubbles. The first diagram (a) shows a correlation between the volumes of bubbles and melt inclusions. The linear correlation implies a homogeneous trapping. The inclusion K7b (Fig. 2), strongly deviating from the general linear trend (a bubble occupies 17 vol.% of the inclusion), contains excess fluid and resulted from a heterogeneous trapping (melt + fluid). For comparison, the volumes obtained from 2D and 3D measurements are presented. For 2D measurements, two estimates are made: under assumption that the thickness of melt inclusion is equal to its width ( $z = y$ ) (Moore et al., 2015) or that the volume of melt inclusion can be estimated as the volume of a sphere with a diameter equal to the average linear diameter of the inclusion ( $d = x/2 + y/2$ ) (Mironov et al., 2015). The second approach yields smaller values for the bubble volume. One more estimate (not shown in the plot), when the thickness of melt inclusion is taken to be equal to the average of the length and width ( $z = x/2 + y/2$ ) (Tucker et al., 2019), virtually coincides with the volume of a spherical melt inclusion (Table 1). For 3D measurements,  $z_2$  corresponds to the thickness of melt inclusion in the orthogonal cross section. Dark squares mark inclusions with the maximum content of  $\text{CO}_2$  in the bubble ( $\sim 0.45$  wt.%, see also Fig. 5 and Table 1) among homogeneously trapped melt inclusions. The second diagram (b) shows correlation between the relative volumes of bubbles in melt inclusions estimated by two alternative 3D measurement methods. The volumes estimated from the melt inclusions thickness measured in the orthogonal cross sections ( $z_2$ ) are plotted along the  $X$  axis, and the volumes estimated from the optical data on the inclusion thickness ( $z_1$ ) are plotted along the  $Y$  axis.

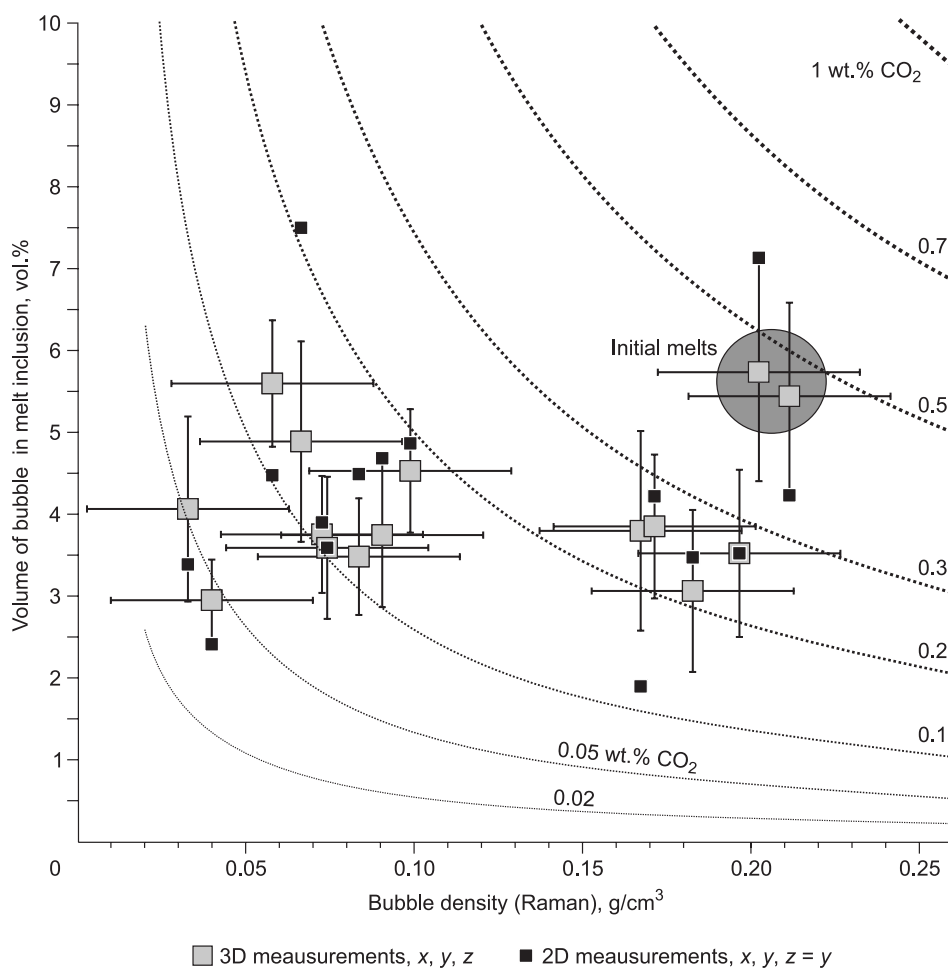


**Fig. 5.** The content of CO<sub>2</sub> in the gas phase of melt inclusion depending on its density and relative volume. Large squares mark the results of mass balance calculation of the CO<sub>2</sub> content in the gas bubbles of melt inclusions from the Karymsky Volcano. They show the minimum bulk contents of CO<sub>2</sub> in the melt inclusions and trapped melts. The wide range of the CO<sub>2</sub> contents (0.05–0.45 wt.%) can be explained by the variable degassing of parental magmas with ~0.45 wt.% CO<sub>2</sub>. The error in the density estimation ( $2\sigma$ ) is  $\pm 0.03$  g/cm<sup>3</sup>, which includes an external error of 0.02 g/cm<sup>3</sup> in (Moore et al., 2018) and the average reproducibility of reference samples in this study (0.011 g/cm<sup>3</sup>) (Fig. 3). The error in the estimation of the relative bubble volume is based on the errors in determination of the absolute volumes of melt inclusions and their bubbles. The errors in volume estimation were calculated by the formula  $errV = V \cdot \pi/2 \cdot d^2 \cdot errL$ , where  $errV$  is the absolute error for the volume of melt inclusion or fluid bubble,  $\pi = 3.14$  (Pi-number),  $d$  is the average diameter of melt inclusion  $(x/3 + y/3 + z/3)$  or fluid bubble, and  $errL$  is the error in the measurements of linear dimensions ( $\pm 2$   $\mu$ m for melt inclusion and  $\pm 0.5$   $\mu$ m for bubble). The error in the relative bubble volume was then calculated using in standard rule of error propagation. For the ellipsoid  $(x, y, z)$ ,  $z$  is taken as  $z/2$ , i.e., the thickness of melt inclusion in the orthogonal cross section. For comparison, we present data for the case when the thickness of melt inclusion is not measured but is taken equal to its width ( $z = y$ ) (Table 1).

exceeding the “critical” values of 6–8 vol.% (Aster et al., 2016) suggest a homogeneous composition (melt) of the trapped melt inclusions (Fig. 4a).

Comparison of the melt inclusion volumes estimated from the results of 3D  $(x, y, z)$  and 2D  $(x, y, z = y)$  measurements shows a significant and nonsystematic error in the estimation of the bubble volume fraction in the latter case (Fig. 4a). The difference between the two alternative volume estimates can be as large as 2.6 vol.% (Table 1). This will also strongly affect the estimate of the CO<sub>2</sub> content in the gas bubbles of melt inclusions (Fig. 5). In the 2D measurements, the minimum gas bubble volume is obtained under assumption of a spherical melt inclusion, i.e., when its diameter is equal to the average of its length and width ( $d =$

$x/2 + y/2$ ) (Fig. 4a; Table 1). Similar results are obtained when the thickness of melt inclusion is taken to be the average of its length and width ( $z = x/2 + y/2$ ) (Tucker et al., 2019) (Table 1). Comparison of the bubble volumes estimated from the results of optical measurements of melt inclusion thickness ( $z1$ ) and measurements in the orthogonal cross sections ( $z2$ ) (i.e., two alternative 3D measurements) shows good agreement (Fig. 4b). Their values are within the error in the estimation of the relative volumes of gas bubbles of the melt inclusions, and the difference between the two estimates varies from 0 to 0.8 vol.% (not exceeding 10 rel.%), averaging 0.4 vol.% (Fig. 4b; Table 1).

This study shows that a correct estimation of the bulk content of CO<sub>2</sub> in melt inclusions and, accordingly, in the



parental melts requires a direct 3D measurement of the linear sizes of the melt inclusions. To elaborate the most effective and precise method for estimating the melt inclusion volume, it is important to compare the calculated volumes of melt inclusions as ellipsoids (as in this paper) and the real volumes of the melt inclusions. The real volumes can be estimated by either X-ray microtomography (Creon et al., 2018) or 3D mapping using Raman spectroscopy (<https://www.horiba.com>) for melt inclusions of different shapes in olivine.

#### Density and weight content of CO<sub>2</sub> in the gas phase.

The density of gas bubbles in the studied melt inclusions, calculated from the obtained calibration plot (Fig. 3), varies from 0.03 to 0.25 g/cm<sup>3</sup> (Fig. 5, Table 1). The bubbles can be tentatively divided by density into two groups: (1) bubbles with a density of <0.1 g/cm<sup>3</sup> and a calculated CO<sub>2</sub> content of <0.2 wt.% and (2) bubbles with a density of 0.17–0.21 g/cm<sup>3</sup> and a calculated CO<sub>2</sub> content of >0.2 wt.% (Fig. 5). The maximum CO<sub>2</sub> content in the bubble (0.45 wt.%) was found in two melt inclusions from two olivine grains (K7c and K13, Table 1), with a fluid phase density of 0.20–0.21 g/cm<sup>3</sup>. The fact that the olivine hosting these melt inclusions is the most magnesian (primitive) and the gas bubbles have the largest relative volume indicates that these inclusions are the earliest among the trapped melts of the studied series. The bubble in the melt inclusion K7b is anomalously large (17 rel.%) and has a maximum density (0.25 g/cm<sup>3</sup>) and, accordingly, an abnormally high calculated content of CO<sub>2</sub> (1.9 wt.%). That is, this inclusion, in contrast to the other in the same sample, resulted from a heterogeneous trapping of melt and CO<sub>2</sub>-rich fluid. The inclusion evidences that it was trapped by an olivine phenocryst crystallizing from CO<sub>2</sub>-saturated melt. The exact compositions of the host olivine and the melt inclusion glass have not yet been determined. Hence, it is not clear which stage of crystallization of olivine (K7) this particular melt inclusion belongs to, as this olivine phenocryst contains two other melt inclusions: inclusion K7c with a high CO<sub>2</sub> content in bubble (0.45 wt.%, host Ol Fo<sub>88.4</sub>) and inclusion K7a with a much lower CO<sub>2</sub> content (0.11 wt.%) (Figs. 1a and 5; Table 1).

## DISCUSSION AND SOME PETROLOGICAL IMPLICATIONS

The observed variations in the CO<sub>2</sub> content in the gas bubbles of melt inclusions (0.45–0.05 wt.%) (Fig. 5; Table 1) might be due to olivine crystallization and trapping of melts variably depleted in CO<sub>2</sub> during the magma ascent and degassing. The least degassed were melts represented by two melt inclusions, K7c and K13, with the calculated CO<sub>2</sub> content of ~0.45 wt.% in the bubbles (Fig. 5; Table 1). This value can be taken as the minimum initial content of CO<sub>2</sub> in the parental melts of the Karymsky Volcano.

The estimated contents of CO<sub>2</sub> (0.45 wt.%, this work) and H<sub>2</sub>O (~ 4.5 wt.% (Tobelko et al., 2019)) in the parental

melts of the Karymsky Volcano and the application of the CO<sub>2</sub> and H<sub>2</sub>O solubility models (Shishkina et al., 2010; Duan, 2014) allow estimation of the minimum pressures at which the crystallization of the melts and their fluid saturation began. According to the H<sub>2</sub>O–CO<sub>2</sub> solubility model (Duan, 2014), these pressures are estimated at 7–8 kbar for the average composition of the Karymsky Volcano parental melt (Tobelko et al., 2019). Knowing the Kamchatka crust density  $\rho$  (kg/m<sup>3</sup>), we can calculate the depth of crystallization,  $h$  (m), from the equation  $P = \rho \cdot g \cdot h$ , where  $P$  is pressure (Pa) and  $g$  is free-fall acceleration (9.8 m/s<sup>2</sup>). The average density of the upper 30 km crust in the Eastern volcanic belt of Kamchatka, ~2.8 g/cm<sup>3</sup> (~2800 kg/m<sup>3</sup>), was calculated from the data presented by Nurmukhamedov et al. (2016) for the eastern part of the profile 3–3' north of the Avachinsky group of volcanoes: a depth of 0–2 km — 2.66 g/cm<sup>3</sup>, 2–8 km — 2.72 g/cm<sup>3</sup>, 8–20 km — 2.73 g/cm<sup>3</sup>, and 20–30 km — 2.95 g/cm<sup>3</sup>. Thus, for the obtained crust density, a pressure of 1 kbar (0.1 GPa) corresponds to a depth of 3.64 km. Accordingly, the minimum pressure of crystallization of the Karymsky Volcano parental melts, 7 kbar, corresponds to a depth of ~25 km.

The estimated depths of the beginning of parental-melt crystallization (>25 km) are consistent with the data on seismicity beneath the Karymsky volcanic center. For example, seismic events occur at a depth of <20 km during the quiescent periods of the Karymsky Volcano, while during its eruption (as in 1996), seismic events were recorded at depths of 60–20 km (Gordeev et al., 1998; Zobin et al., 2003). These deep events seem to be related to the transport of the parental volcanic magmas, which begin to crystallize in this depth interval. Similar estimates of the initial crystallization pressure were obtained by different methods for other volcanoes of Kamchatka: Avachinsky, Klyuchevskoi, and Tolbachik (Portnyagin et al., 2005; Mironov et al., 2015; Mironov and Portnyagin, 2018), which perfectly matches the seismotomographic data on the presence of magmas at the mentioned depths (Koulakov et al., 2017). This suggests that the parental magmas of the Eastern volcanic belt of Kamchatka began to crystallize at least in the lower mafic crust or in the mantle (Balesta and Gontovaya, 1985; Nurmukhamedov et al., 2016; Koulakov et al., 2017).

## CONCLUSIONS

In the course of the study, the dependence between the CO<sub>2</sub> density and the distance between the characteristic CO<sub>2</sub> Raman lines (Fermi diads) was calibrated with a Horiba LabRam HR800 Raman spectrometer at the Sobolev Institute of Geology and Mineralogy, Novosibirsk. This dependence is described by the equation  $\rho_{\text{CO}_2} \text{ (g/cm}^3\text{)} = 0.3776 \times \Delta F \text{ (cm}^{-1}\text{)} - 38.851$ . Study of a series of olivine-hosted melt inclusions from the Karymsky Volcano has demonstrated how this dependence can be used for the estimation of gas bubble densities and initial CO<sub>2</sub> contents in melt inclusions and parental magmas.

The data obtained can be used as a basis for regional works to estimate the initial CO<sub>2</sub> content in parental island-arc magmas and their crystallization pressure and degree of degassing and to establish the relationship between the CO<sub>2</sub> content in magmas and their origin conditions. To improve the Raman spectroscopy method of estimation of the initial content of CO<sub>2</sub> in melt inclusions and the mass balance calculation technique, we propose to carry out a preliminary high-temperature experiment on the complete remelting of daughter phases in melt inclusions and to perform more accurate optical 3D measurements of the melt inclusion size.

#### ACKNOWLEDGEMENTS

The studied sample of basalt from the Karymsky Volcano was kindly provided by E.N. Grib. The authors are grateful to the reviewers V.B. Naumov, Institute of Geochemistry and Analytical Chemistry (GEOKhI), Moscow and A.A. Tomilenko, Institute of Geology and Mineralogy (IGM), Novosibirsk for valuable comments, and I.A. Kupriyanov (IGM) for instrumental tuning for Raman spectroscopy studies.

The research was supported by grants 17-35-50081 and 19-05-00934 from the Russian Foundation for Basic Research (RFBR). D.P. Tobelko and S.P. Krashennnikov are also grateful to RFBR for their personal support within this work (grants 18-35-00529 and 18-35-00497). The experimental study of melt inclusions and the use of Raman spectroscopy were supported by the budget funding of GEOKhI and IGM, respectively.

#### REFERENCES

- Aster, E.M., Wallace, P.J., Moore, L.R., Watkins, J., Gazel, E., Bodnar, R.J., 2016. Reconstructing CO<sub>2</sub> concentrations in basaltic melt inclusions using Raman analysis of vapor bubbles. *J. Volcanol. Geotherm. Res.* 323, 148–162.
- Bakker, R.J., Diamond, L.W., 2006. Estimation of volume fractions of liquid and vapor phases in fluid inclusions, and definition of inclusion shapes. *Am. Mineral.* 91, 635–657.
- Balesta, S.T., Gontovaya, L.I., 1985. Crustal structure in the Kamchatkan segment of the Pacific transition zone. *J. Geodynam.* 3 (3–4), 245–257.
- Blank, J.G., Brooker, R.A., 1994. Experimental studies of carbon dioxide in silicate melts; solubility, speciation, and stable carbon isotope behavior. *Rev. Mineral. Geochem.* 30 (1), 157–186.
- Bucholz, C.E., Gaetani, G.A., Behn, M.D., Shimizu, N., 2013. Post-entrapment modification of volatiles and oxygen fugacity in olivine-hosted melt inclusions. *Earth Planet. Sci. Lett.* 374, 145–155.
- Creon, L., Levresse, G., Remusat, L., Bureau, H., Carrasco-Nunez, G., 2018. New method for initial composition determination of crystallized silicate melt inclusions. *Chem. Geol.* 483, 162–173.
- Danyushevsky, L., McNeill, A.W., Sobolev, A.V., 2002. Experimental and petrological studies of melt inclusions in phenocrysts from mantle-derived magmas: an overview of techniques, advantages and complications. *Chem. Geol.* 183, 5–24.
- Duan, X.Z., 2014. A general model for predicting the solubility behavior of H<sub>2</sub>O-CO<sub>2</sub> fluids in silicate melts over a wide range of pressure, temperature and compositions. *Geochim. Cosmochim. Acta* 125, 582–609.
- Fall, A., Tattitch, B., Bodnar, R.J., 2011. Combined microthermometric and Raman spectroscopic technique to determine the salinity of H<sub>2</sub>O–CO<sub>2</sub>–NaCl fluid inclusions based on clathrate melting. *Geochim. Cosmochim. Acta* 75 (4), 951–964.
- Frezzotti, M.L., 2001. Silicate-melt inclusions in magmatic rocks: applications to petrology. *Lithos* 55, 273–299.
- Frezzotti, M.L., Tecce, F., Casagli, A., 2012. Raman spectroscopy for fluid inclusion analysis. *J. Geochem. Explor.* 112, 1–20.
- Grib, E.N., Perepelov, A.B., 2008. Olivine basalts at the Karymsky volcanic center: mineralogy, petrogenesis, and magma sources. *J. Volcanol. Seismol.* 2 (4), 228–247.
- Gordeev, E.I., Droznin, D.V., Kasahara, M., Levina, V.I., Leonov, V.L., Miyamachi, H., Okayama, M., Saltykov, V.A., Sinitsyn, V.I., Cheburov, V.N., 1998. Seismic events associated with the 1996 volcanic eruptions in the Karymsky volcanic center. *Volcanol. Seismol.* 19, 713–735.
- Hartley, M.E., MacLennan, J., Edmonds, M., Thordarson, T., 2014. Reconstructing the deep CO<sub>2</sub> degassing behaviour of large basaltic fissure eruptions. *Earth Planet. Sci. Lett.* 393, 120–131.
- <https://www.horiba.com/at/scientific/products/raman-spectroscopy/raman-imaging/3d-confocal-volume-imaging/>
- Kamenetsky, V.S., Davidson, P., Mernagh, T.P., Crawford, A.J., Gemmell, J.B., Portnyagin, M.V., Shinjo, R., 2002. Fluid bubbles in melt inclusions and pillow-rim glasses: high-temperature precursors to hydrothermal fluids? *Chem. Geol.* 183, 349–64.
- Koulakov, I., Abkadyrov, I., Al Arifi, N., Deev, E., Droznina, S., Gordeev, E.I., Jakovlev, A., El Khrepy, S., Kulakov, R.I., Kugaenko, Y., Novgorodova, A., Senyukov, S., Shapiro, N., Stupina, T., West, M., 2017. Three different types of plumbing system beneath the neighboring active volcanoes of Tolbachik, Bezymianny, and Klyuchevskoy in Kamchatka. *J. Geophys. Res. Solid Earth* 122 (5), 3852–3874.
- Krashennnikov, S.P., Sobolev, A.V., Batanova, V.G., Kargaltsev, A.A., Borisov, A.A., 2017. Experimental testing of olivine–melt equilibrium models at high temperatures. *Dokl. Earth Sci.* 475 (2), 919–922.
- Krashennnikov, S.P., Sobolev, A.V., Asafov, E.V., Kargaltsev, A.A., Borisov, A.A., 2018. Routine technique of homogenization of melt inclusions in minerals in a high-temperature vertical tube furnace under the atmospheric pressure, in: All-Russian Annual Seminar on Experimental Mineralogy, Petrology, and Geochemistry (VES-EMPG-2018), Moscow, 18–19 April 2018 [in Russian]. GEOKhI RAN, Moscow, p. 82.
- Lamadrid, H.M., Moore, L. R., Moncada, D., Rimstidt, J. D., Burrows, R.C., Bodnar, R. J., 2017. Reassessment of the Raman CO<sub>2</sub> densimeter. *Chem. Geol.* 450, 210–222.
- Mironov, N.L., Portnyagin, M.V., 2011. H<sub>2</sub>O and CO<sub>2</sub> in parental magmas of Kliuchevskoi volcano inferred from study of melt and fluid inclusions in olivine. *Russian Geology and Geophysics (Geologiya i Geofizika)* 52 (11), 1353–1367 (1718–1735).
- Mironov, N.L., Portnyagin, M.V., 2018. Coupling of redox conditions of mantle melting and copper and sulfur contents in primary magmas of the Tolbachinsky Dol (Kamchatka) and Juan de Fuca Ridge (Pacific Ocean). *Petrology* 26 (2), 145–166.
- Mironov, N., Portnyagin, M., Botcharnikov, R., Gurenko, A., Hoernle, K., Holtz, F., 2015. Quantification of the CO<sub>2</sub> budget and H<sub>2</sub>O-CO<sub>2</sub> systematics in subduction-zone magmas through the experimental hydration of melt inclusions in olivine at high H<sub>2</sub>O pressure. *Earth Planet. Sci. Lett.* 425, 1–11.
- Moore, L.R., Bodnar, R.J., 2019. A pedagogical approach to estimating the CO<sub>2</sub> budget of magmas. *J. Geol. Soc.* 176 (2), 398–407.
- Moore, L.R., Gazel, E., Tuohy, R., Lloyd, A. S., Esposito, R., Steele-MacInnis, M., Hauri, E. H., Wallace, P. J., Plank, T., Bodnar, R. J., 2015. Bubbles matter: An assessment of the contribution of vapor bubbles to melt inclusion volatile budgets. *Am. Mineral.* 100 (4), 806–823.
- Moore, L.R., Mironov, N.L., Portnyagin, M.V., Gazel, E., Bodnar, R.J., 2018. Volatile contents of primitive bubble-bearing melt inclusions

- from Klyuchevskoy volcano, Kamchatka: Comparison of volatile contents determined by mass-balance versus experimental homogenization. *J. Volcanol. Geotherm. Res.* 358, 124–131.
- Naumov, V.B., Portnyagin, M.V., Tolstykh, M.L., Yarmolyuk, V.V., 2006. Chemical composition and crystallization conditions of trachybasalts from the Dzhida field, Southern Baikal volcanic area: Evidence from melt and fluid inclusions. *Geochem. Int.* 44 (3), 286–295.
- Naumov, V.B., Dorofeeva, V.A., Tolstykh, M.L., Giris, A.V., Yarmolyuk, V.V., 2020. Composition and geochemical specifics of Kamchatka magmatic melts based on the analysis of melt inclusions and quenched Glasses of Rocks. *Geochem. Int.* 58 (3), 271–290.
- Nurmukhamedov, A.G., Nedyadko, V.V., Rakitov, V.A., Lipatyev, M.S., 2016. The lithosphere boundaries in Kamchatka based on data on the earthquake converted-wave method (ECWM). *Vestnik KRAUNTs. Nauki o Zemle* 29 (1), 35–52.
- Portnyagin, M.V., Mironov, N.L., Matveev, S.V., Plechov, P.Yu., 2005. Petrology of avachites, high-magnesian basalts of Avachinsky Volcano, Kamchatka: II. Melt inclusions in olivine. *Petrology* 13 (4), 322–351.
- Portnyagin, M., Hoernle, K., Plechov, P., Mironov, N., Khubunaya, S., 2007. Constraints on mantle melting and composition and nature of slab components in volcanic arcs from volatiles (H<sub>2</sub>O, S, Cl, F) and trace elements in melt inclusions from the Kamchatka Arc. *Earth Planet. Sci. Lett.* 255 (1–2), 53–69.
- Robidoux, P., Frezzotti, M.L., Hauri, E.H., Aiuppa, A., 2018. Shrinkage bubbles: The C-O-H-S magmatic fluid system at San Cristóbal volcano. *J. Petrol.* 59 (11), 2093–2122.
- Schiano, P., 2003. Primitive mantle magmas recorded as silicate melt inclusions in igneous minerals. *Earth Sci. Rev.* 63 (1–2), 121–144.
- Shishkina, T.A., Botcharnikov, R.E., Holtz, F., Almeev, R.R., Portnyagin, M.V., 2010. Solubility of H<sub>2</sub>O- and CO<sub>2</sub>-bearing fluids in tholeiitic basalts at pressures up to 500 MPa. *Chem. Geol.* 277 (1–2), 115–125.
- Sobolev, A.V., 1996. Melt inclusions in minerals as a source of principle petrological information. *Petrology* 4 (3), 209–220.
- Steele-Macinnis, M., Esposito, R., Bodnar, R.J., 2011. Thermodynamic model for the effect of post-entrapment crystallization on the H<sub>2</sub>O–CO<sub>2</sub> systematics of vapor-saturated silicate melt inclusions. *J. Petrol.* 52 (12), 2461–2482.
- Taracsak, Z., Hartley, M.E., Burgess, R., Edmonds, M., Iddon, F., Longpre, M.A., 2019. High fluxes of deep volatiles from ocean island volcanoes: Insights from El Hierro, Canary Islands. *Geochim. Cosmochim. Acta* 258, 19–36.
- Tingle, T.N., Green, H.W., Finnerty, A.A., 1988. Experiments and observations bearing on the solubility and diffusivity of carbon in olivine. *J. Geophys. Res. Solid Earth* 93 (B12), 15289–15304.
- Tobelko, D.P., Portnyagin, M.V., Krashenninikov, S.P., Grib, E.N., Plechov, P.Yu., 2019. Compositions and formation conditions of primitive magmas of the Karymsky volcanic center, Kamchatka: evidence from melt inclusions and trace-element Thermobarometry. *Petrology* 27, 243–264.
- Tucker, J.M., Hauri, E.H., Pietruszka, A.J., Garcia, M.O., Marske, J.P., Trusdell, F.A., 2019. A high carbon content of the Hawaiian mantle from olivine-hosted melt inclusions. *Geochim. Cosmochim. Acta* 254, 156–172.
- Wallace, P.J., 2005. Volatiles in subduction zone magmas: concentrations and fluxes based on melt inclusion and volcanic gas data. *J. Volcanol. Geotherm. Res.* 140 (1–3), 217–240.
- Wallace, P., Kamenetsky, V.S., Cervantes, P., 2015. Melt inclusion CO<sub>2</sub> contents, pressures of olivine crystallization and the problem of shrinkage bubbles. *Am. Mineral.* 100 (4), 787–794.
- Wang, X.L., Chou, I.M., Hu, W.X., Burruss, R.C., Sun, Q., Song, Y.C., 2011. Raman spectroscopic measurements of CO<sub>2</sub> density: Experimental calibration with high-pressure optical cell (HPOC) and fused silica capillary capsule (FSCC) with application to fluid inclusion observations. *Geochim. Cosmochim. Acta* 75 (14), 4080–4093.
- Zobin, V.M., Levina, V.I., Maguskin, M.A., 2003. Seismicity and crustal deformation preceding the January 1996 eruptions at Karymsky Volcanic Center, Kamchatka. *Bull. Volcanol.* 65, 477–485.

*Editorial responsibility:* N.V. Sobolev